Spatiotemporal rogue events in femtosecond filamentation

D. Majus,[1] V. Jukna,[1] G. Valiulis,[1] D. Faccio,[2] and A. Dubietis[1,*]

[1]*Department of Quantum Electronics, Vilnius University, Saulėtekio Avenue 9, Building 3, LT-10222 Vilnius, Lithuania*

[2]*School of Engineering and Physical Sciences, SUPA, Heriot-Watt University, Edinburgh EH14 4AS, United Kingdom*

(Received 17 November 2010; published 23 February 2011)

We present experimental and numerical investigations of optical extreme (rogue) event statistics recorded in the regime of femtosecond pulse filamentation in water. In the spectral domain, the extreme events manifest themselves as either large or small extremes of the spectral intensity, justified by right- or left-tailed statistical distributions, respectively. In the time domain, the observed extreme events are associated with pulse splitting and energy redistribution in space and therefore are exquisitely linked to three-dimensional, spatiotemporal dynamics and formation of the *X* waves.

DOI: 10.1103/PhysRevA.83.025802 PACS number(s): 42.65.Jx, 42.65.Sf

Rogue or freak waves are well known in hydrodynamics and refer to statistically rare giant waves that occur on the surface of oceans and seas (see, e.g., [1] for a review). From a general point of view, rogue waves or, more generally, rogue (extreme) events represent an extreme sensitivity of the nonlinear system to the initial conditions. Indeed, recently rogue-wave-like behavior was shown to be inherent to diverse nonlinear physical environments: propagation of acoustic waves in superfluid helium [2], variation of local atomic density in Bose-Einstein condensates [3], ion-acoustic and Alfvén wave propagation in plasmas [4], and propagation of acoustic-gravity waves in the atmosphere [5].

Optical rogue waves, recently discovered by Solli *et al.* [6], constitute a fascinating topic in modern nonlinear optics [7,8]. At present, most of the knowledge on optical rogue waves is brought by the studies of the supercontinuum generation in optical fibers, under a variety of operating conditions and propagation regimes ranging from CW to femtosecond pulses [9–15], and has been shown to share a great similarity with the waves' hydrodynamical counterparts [16]. In fibers, rogue waves represent rare soliton pulses, whose statistics are characterized by extreme-value (non-Gaussian or, more specifically, L-shaped) distributions. It is generally accepted that optical rogue waves emerge as a result of the nonlinear wave interactions and soliton collisions, although the precise underlying physical mechanisms leading to their formation are still under debate [17].

Extreme-value statistics are also inherent to various nonlinear optical systems, where dimensionality and nonlinear wave dynamics are more complex compared to optical fibers: nonlinear optical cavities [18], nonlinear optical lattices [19], nonlinear waveguides [20], and ultrashort pulse filamentation [21]. Ultrashort pulse filamentation is of particular interest, since it represents an ultimate regime of light and matter interaction, and the nonlinear dynamics is governed by the interplay of self-focusing and self-phase modulation, white-light continuum generation, diffraction, nonlinear absorption, free-electron plasma generation, and space-time effects [22]. On the other hand, filamentation phenomena find a broad spectrum of applications, ranging from atmospheric analysis [23] to laser micromachining [24], and therefore the stability issues of the filaments are of primary importance.

In this Brief Report, we report on a class of optical rogue events that occur in three-dimensional geometries as opposed to the widely studied one- or two-dimensional systems. In three-dimensional space, strong space-time coupling may lead to rogue events that bear some specific features, namely a trailing peak with a lower-than-average intensity albeit with a wider spectrum. We show that these extreme events are associated to *X*-wave formation in the normal group-velocity-dispersion regime, as opposed to the temporal solitons observed in the anomalous regime in optical fibres.

In the experiment, we used an amplified Ti:sapphire laser system that delivers 130-fs pulses at $\lambda_0 = 800$ nm. The laser beam was attenuated and loosely focused by an $f = 500$ mm lens down to 60 μm full width at half maximum (FWHM) diameter at the input face of the 43-mm-long water-filled cuvette. The input energy of 0.61 μJ (which equates to 1.23 P_{cr}, $P_{cr} = 3.77\lambda_0^2/(8\pi n_0 n_2) = 3.8$ MW, where $n_0 = 1.328$ and $n_2 = 1.9 \times 10^{-16}$ cm^2/W [25] are linear and nonlinear refractive indexes of water at 800 nm) was chosen so as to excite a single filament, whose occurrence was verified by the white-light spectrum at the exit of the nonlinear medium, and to uncover early spatiotemporal dynamics not altered by propagation and other nonlinear effects. The spectrum of the filament was collected using a short-focal-distance ($f = 30$ mm) lens and, after passing several neutrally scattering layers of thin teflon film, was directed to a fiber spectrometer with a 16-bit detector (Ocean Optics), which has a spectral detection range from 200 to 950 nm. The statistical distribution of the input-pulse energy was almost perfectly Gaussian, with a standard deviation of $\leqslant 1\%$.

The occurrence of extreme events in the filamentation regime is readily observable in the extreme-value statistics of the spectral intensity, which exhibits a characteristic L-shaped distribution. Figure 1(a) illustrates the statistics of 5000 experimentally recorded single-shot spectra measured at $1.23P_{cr}$. Multiple gray curves show the individual single-shot spectra, whose average spectral intensity profile is overplotted by a black curve. The widest and the narrowest spectra are highlighted by the red and blue curves, respectively, while the dashed curve indicates the input-pulse spectrum.

*Corresponding author: audrius.dubietis@ff.vu.lt

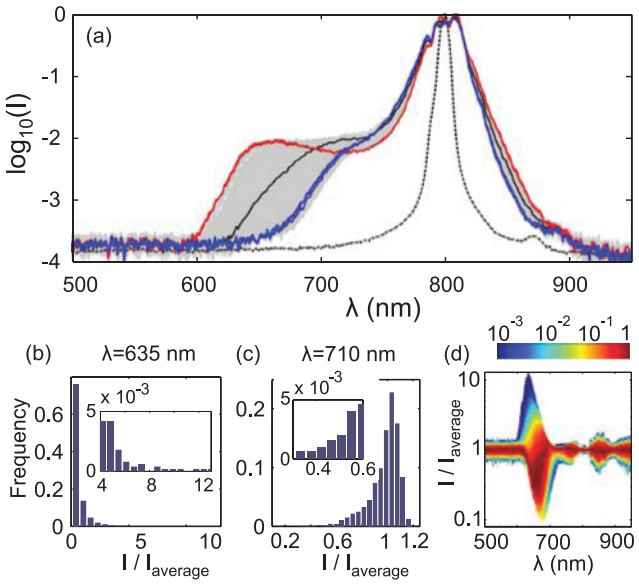

FIG. 1. (Color online) (a) The 5000 experimentally measured single-shot spectra of the filament (gray curves) recorded at $1.23P_{cr}$. The average spectrum is shown by the black curve, the widest and the narrowest extremes are highlighted by the red and blue curves, respectively, while the input spectrum is plotted by the dashed curve. Frequency distributions of the spectral intensity at: (b) 635 nm and (c) 710 nm. Insets show a magnified portion of the long tails. (d) Statistics of the spectral intensity across the entire spectral detection range.

A more detailed statistical analysis of these spectra is presented in Figs. 1(b) and 1(c) by plotting the frequency distribution of the spectral intensity at particular wavelengths of 635 and 710 nm, respectively. At 635 nm, the spectral intensity exhibits a clear right-tailed distribution. The spectral intensity of the most prominent extreme events is more than 10 times larger than the average, as seen from the inset, which highlights the extended tail. Interestingly, at 710 nm, the L-shaped distribution is left-tailed, i.e., showing that in the same data set there are a number of events exposing small-intensity extremes. A closer look at Fig. 1(a) reveals that these marginal spectra have different shapes: those with the highest spectral intensity at 650 nm exhibit a dip around 710 nm, and vice versa. Hence, the observed statistics at different wavelengths is determined by the change of the spectral shape due to correlation between frequency components that occur in the self-phase modulation-induced spectral broadening [26]. Figure 1(d) combines the statistics of the spectral intensity across the entire spectral detection range, where (logarithmic) color coding renders the normalized frequency of the spectral intensity at a particular wavelength. Notice that distinct extreme events occur mostly on the blueshifted side of the spectrum.

In what follows, we quantitatively reproduce the experimental results and characterize the spatiotemporal structure of the extreme events by the use of numerical simulations. We solve the extended nonlinear Schrödinger equation, which in the spectral domain reads as

$$\frac{\partial S(\Omega,k_\perp)}{\partial z} + iD(\Omega,k_\perp)S(\Omega,k_\perp) = S_N(\Omega,k_\perp), \qquad (1)$$

where z is the longitudinal coordinate, $\Omega = \omega - \omega_0$ is the frequency detuning from the carrier frequency ω_0, and $k_\perp$ is the transverse wave number. The function $D(\Omega,k_\perp)$ describes linear propagation and accounts for diffraction in the nonparaxial case, full dispersion for distilled water [27], and linear absorption:

$$D(\Omega,k_\perp) = \sqrt{k(\omega_0+\Omega)^2 - k_\perp^2} - k_0 - \frac{\Omega}{v_g} - i\alpha(\Omega), \qquad (2)$$

where $v_g = \frac{\partial\omega}{\partial k}|_{\omega_0}$ is the group velocity of the pulse, $k(\omega) = \omega n(\omega)/c$ is the wave number, $k_0 = k(\omega_0)$, and $\alpha(\Omega)$ is the absorption coefficient, whose values in the visible and infrared were combined using data from [28,29]. The complex amplitude of the pulse $A(t,r,z)$ and $S(\Omega,k_\perp)$ are related via Fourier and Hankel transforms:

$$A(t,r,z) = \int_{-\infty}^{+\infty}\int_0^{+\infty} S(\Omega,k_\perp)e^{i\Omega t}J_0(k_\perp r)k_\perp\, dk_\perp \frac{d\Omega}{2\pi}, \qquad (3)$$

where t is the temporal coordinate corresponding to the frame of reference moving with the group velocity of the pulse and r is the radial coordinate. $S_N(\Omega,k_\perp)$ is the spectral representation of the nonlinear terms:

$$S_N(\Omega,k_\perp) = \int_{-\infty}^{+\infty}\int_0^{+\infty} N(t,r)e^{-i\Omega t}J_0(k_\perp r)r\, dr\, dt \qquad (4)$$

where

$$N(t,r) = \frac{i\omega_0 n_2}{c}|A|^2A - \frac{n_2}{c}\frac{\partial}{\partial t}(|A|^2A) - \frac{\beta^{(K)}}{2}|A|^{2K-2} - \frac{\sigma}{2}(1-i\omega_0\tau_c)\rho A. \qquad (5)$$

The terms on the right-hand side describe the instantaneous Kerr effect, self-steepening, multiple photon absorption, and the effect of free-electron plasma; $K = 5$ is the order of the multiphoton absorption, assuming $E_g = 6.5$ eV and a single photon energy $\hbar\omega_0 = 1.5$ eV; $\beta^{(K)}$ is the multiphoton absorption coefficient, taken as $\beta^{(5)} = 1.1\times10^{-51}$ cm^7/W^4; ρ is the free-electron density; $\sigma = 4.7\times10^{-22}$ m^2 is the cross section for electron-neutral inverse bremsstrahlung; and $\tau_c = 3$ fs [30] is the electronic collision time in the conduction band. The values of $\beta^{(5)}$ and σ were evaluated using the formalism described in [31], and the plasma dynamics was accounted for in the same manner as in [32], including multiphoton and avalanche ionization and neglecting electron diffusion and recombination owing to sufficiently longer lifetime of the electron plasma as compared to the pulse width [33]. The calculations were performed for an input Gaussian pulsed beam with 60 μm diameter, $t_p = 130$ fs FWHM pulse width, central wavelength of $\lambda_0 = 800$ nm, and the input-beam intensity of $I_0 = 130$ GW/cm^2. In order to simulate the output statistics, we have modified the input beam by introducing 2% intensity noise, 0.1% phase noise, and 1% energy noise. The noise has a Gaussian distribution and was implemented using the Box-Muller transform of uniformly distributed random numbers.

The statistical results obtained by the numerical simulations are shown in Fig. 2. Figure 2(a) illustrates 500 individual axial spectra, and Figs. 2(b) and 2(c) show the statistical distributions of the spectral intensity at 635 and 730 nm, respectively, which are summarized for the entire spectral

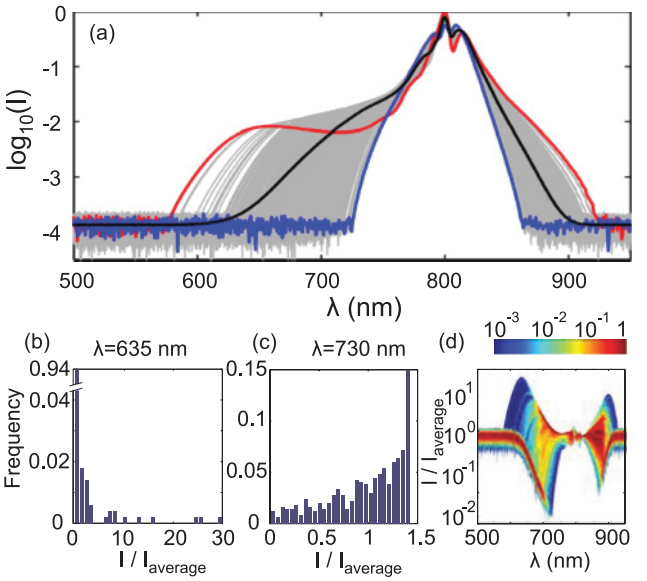

FIG. 2. (Color online) (a) The 500 numerically simulated single-shot spectra (gray curves). Curve designations are the same as in Fig. 1(a). Frequency distributions of the spectral intensity at (b) 635 nm and (c) 730 nm. (d) Statistics of the spectral intensity across the entire wavelength range.

range in Fig. 2(d). Note here that, in the presentation of the numerical results, we have added an artificial noise at the level which corresponds to the experimental detection range of the fiber spectrometer. The numerical data recover almost all the essential statistical features captured experimentally, as shown in Fig. 1.

The relevant question is how the extreme events in the spectral intensity manifest themselves in the space-time domain. We recall that, in the fiber environment, rogue waves are associated with the redshifted soliton pulses of extreme amplitude, which emerge in the region of anomalous group-velocity dispersion. However, the temporal dynamics in the femtosecond filamentation is different: the spectral broadening during self-focusing of the ultrashort light pulses in a medium with normal group-velocity dispersion is linked to pulse splitting and shock-front dynamics, where the leading shock front is associated with the redshifted axial radiation, and the trailing shock front with the blueshifted axial radiation [34]. A more general view of this concept was proposed in the framework of two split nonlinear X waves, one traveling at subluminal and another at superluminal velocities with respect to the group velocity of the input Gaussian pulse, and whose localization is ensured by the off-axis, conical part of the beam (conical emission) [35–37].

Figures 3(a)–3(c) show the numerically simulated spatiotemporal intensity distributions that correspond to the narrowest, the average, and the widest spectra, respectively, as highlighted in Fig. 2(a), indicating formation of the split X waves. Figures 3(d)–3(f) show the corresponding on-axis temporal intensity profiles, which highlight pulse splitting events and the formation of optical shocks that are recognized by weak and rapidly decaying oscillations at the pulse fronts. Notably, major differences between the three different cases are observed only in the trailing X wave, whose spatiotemporal extent and on-axis

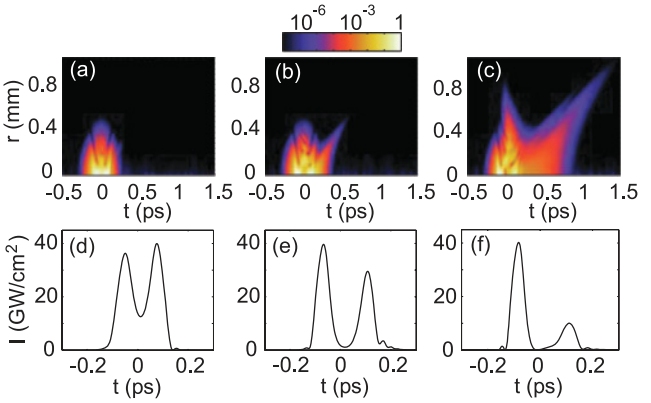

FIG. 3. (Color online) (a)–(c) Spatiotemporal and (d)–(f) on-axis intensity profiles corresponding to the spectra highlighted in Fig. 2(a). See text for details.

intensity exhibit great variability if compared with the leading peak.

This finding was also verified experimentally by measuring the cross-correlation function of the on-axis part of the filament as transmitted through a 40-μm pinhole, imaged and sampled with a short, 30-fs pulse in 20-μm-thick beta barium borate crystal via sum-frequency generation [Fig. 4(a)]. Figures 4(b) and 4(c) compare the numerical and experimental intensity distributions, measured at the time delay of -60 and $+70$ fs [marked by dashed lines in Fig. 4(a)], corresponding to the leading and trailing peaks. The results presented in Figs. 4(b) and 4(c) imply that the variation range of the leading pulse intensity is quite compact; its statistical distribution, aside from a very slight skewness, is similar to the input-intensity variation. In contrast, the intensity of the trailing pulse varies considerably, with clearly expressed left-tailed extreme-value statistics. Given the good agreement between the numerical and experimental data, it is quite surprising that the statistics of the leading and trailing pulses are markedly different, so only the trailing pulse (or, more generally, the overall trailing wave packet) exhibits a rogue-wave-like behavior. We interpret this difference as the result of the X-wave formation under

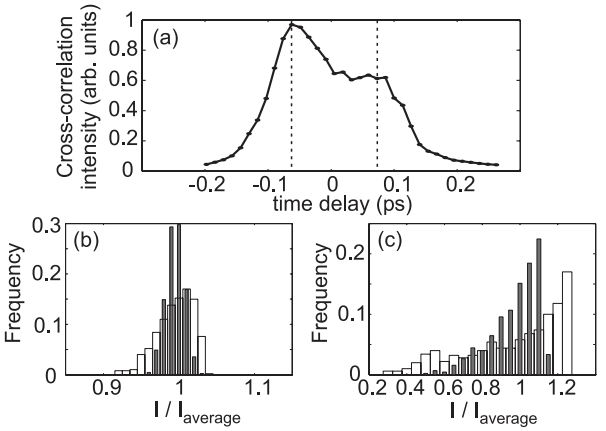

FIG. 4. (a) Experimentally measured cross-correlation function of the on-axis radiation. Numerically simulated (white bars) and experimentally measured (black bars) intensity distributions of the (b) leading and (c) trailing peaks.

the experimental condition addressed: higher-order dispersion and phase-matching in water, and more specifically, water absorption, that increases rapidly toward the infrared [29]. However, the observed peculiarities in dynamics of the red- and blueshifted components require further, extensive study.

In conclusion, under investigated experimental conditions, the extreme events in the femtosecond filamentation regime are identified as large *space-time coupled* intensity fluctuations and formation of an X wave at the trailing edge of the input pulse. The results are significantly different with respect to one-dimensional fiber settings in which extreme events are associated to higher-than-average intensities. The three-dimensional extreme event needs to be visualized in full three-dimensional space rather than in a reduced one-dimensional space: indeed, in Fig. 3(c) we immediately notice that the extreme event is associated to the clear formation of an X wave with largely extended conical tail, i.e., of a truly space-time coupled, three-dimensional wave packet. Due to the ubiquity of space-time coupled effects in three-dimensional systems, we may also expect to observe similar rogue X-wave formation and wave localization events in other settings involving, e.g., acoustic [38] and even seismic waves [39].

[1] K. Dysthe, H. E. Krogstad, and P. Müller, Annu. Rev. Fluid Mech. **40**, 287 (2008).
[2] A. N. Ganshin, V. B. Efimov, G. V. Kolmakov, L. P. Mezhov-Deglin, and P. V. E. McClintock, Phys. Rev. Lett. **101**, 065303 (2008).
[3] Yu. V. Bludov, V. V. Konotop, and N. Akhmediev, Phys. Rev. A **80**, 033610 (2009).
[4] M. S. Ruderman, Eur. Phys. J. Special Topics **185**, 57 (2010).
[5] L. Stenflo and M. Marklund, J. Plasma Phys. **76**, 293 (2010).
[6] D. R. Solli *et al.*, Nature **450**, 1054 (2007).
[7] J. M. Dudley *et al.*, Eur. Phys. J. Spec. Top.**185**, 125 (2010).
[8] B. Jalali *et al.*, Eur. Phys. J. Spec. Top.**185**, 145 (2010).
[9] D. R. Solli, C. Ropers, and B. Jalali, Phys. Rev. Lett. **101**, 233902 (2008).
[10] J. M. Dudley, G. Genty, and B. J. Eggleton, Opt. Express **16**, 3644 (2008).
[11] A. Mussot *et al.*, Opt. Express **17**, 17010 (2009).
[12] M. Erkintalo, G. Genty, and J. M. Dudley, Opt. Lett. **34**, 2468 (2009).
[13] K. Hammani, C. Finot, and G. Millot, Opt. Lett. **34**, 1138 (2009).
[14] B. Kibler, C. Finot, and J. M. Dudley, Eur. Phys. J. Spec. Top. **173**, 273 (2009).
[15] K. Hammani *et al.*, Opt. Express **16**, 16467 (2008).
[16] N. Akhmediev, A. Ankiewicz, and M. Taki, Phys. Lett. A **373**, 675 (2009).
[17] K. Hammani *et al.*, Phys. Lett. A **374**, 3585 (2010).
[18] A. Montina, U. Bortolozzo, S. Residori, and F. T. Arecchi, Phys. Rev. Lett. **103**, 173901 (2009).
[19] A. Maluckov, L. Hadzievski, N. Lazarides, and G. P. Tsironis, Phys. Rev. E **79**, 025601(R) (2009).
[20] Yu. V. Bludov, V. V. Konotop, and N. Akhmediev, Opt. Lett. **34**, 3015 (2009).
[21] J. Kasparian *et al.*, Opt. Express **17**, 12070 (2009).
[22] A. Couairon and A. Mysyrowicz, Phys. Rep. **441**, 47 (2007).
[23] J. Kasparian and J.-P. Wolf, Opt. Express **16**, 466 (2008).
[24] D. Kiselev, L. Woeste, and J.-P. Wolf, Appl. Phys. B **100**, 515 (2010).
[25] Z. W. Wilkes *et al.*, Appl. Phys. Lett. **94**, 211102 (2009).
[26] P. Béjot *et al.*, Appl. Phys. B **87**, 1 (2007).
[27] M. Daimon and A. Masumura, Appl. Opt. **46**, 3811 (2007).
[28] R. M. Pope and E. S. Fry, Appl. Opt. **36**, 8710 (1997).
[29] L. Kou, D. Labrie, and P. Chylek, Appl. Opt. **33**, 3531 (1993).
[30] A. Dubietis *et al.*, Appl. Phys. B **84**, 439 (2006).
[31] J. Noack and A. Vogel, IEEE J. Quantum Electron. **35**, 1156 (1999).
[32] D. Majus, V. Jukna, G. Tamosauskas, G. Valiulis, and A. Dubietis, Phys. Rev. A **81**, 043811 (2010).
[33] S. Minardi *et al.*, Opt. Lett. **33**, 86 (2008).
[34] A. L. Gaeta, Phys. Rev. Lett. **84**, 3582 (2000).
[35] M. Kolesik, E. M. Wright, and J. V. Moloney, Phys. Rev. Lett. **92**, 253901 (2004).
[36] D. Faccio *et al.*, Phys. Rev. Lett. **96**, 193901 (2006).
[37] F. Bragheri *et al.*, Phys. Rev. A **76**, 025801 (2007).
[38] J. Lu and J. F. Greenleaf, IEEE Trans. Ultrason. Ferroelectr. Freq. Control **39**, 441 (1992).
[39] E. Larose, L. Margerin, B. A. van Tiggelen, and M. Campillo, Phys. Rev. Lett. **93**, 048501 (2004).